

1        **Contrasting interannual atmospheric CO<sub>2</sub> variabilities and their**  
2                                    **terrestrial mechanisms for two types of El Niños**

3        Jun Wang<sup>1,2</sup>, Ning Zeng<sup>2,3</sup>, Meirong Wang<sup>4</sup>, Fei Jiang<sup>1</sup>, Jingming Chen<sup>1,5</sup>, Pierre  
4        Friedlingstein<sup>6</sup>, Atul K. Jain<sup>7</sup>, Ziqiang Jiang<sup>1</sup>, Weimin Ju<sup>1</sup>, Sebastian Lienert<sup>8,9</sup>, Julia  
5        Nabel<sup>10</sup>, Stephen Sitch<sup>11</sup>, Nicolas Viovy<sup>12</sup>, Hengmao Wang<sup>1</sup>, Andrew J. Wiltshire<sup>13</sup>

6        <sup>1</sup>International Institute for Earth System Science, Nanjing University, Nanjing, China

7        <sup>2</sup>State Key Laboratory of Numerical Modelling for Atmospheric Sciences and Geophysical Fluid  
8        Dynamics, Institute of Atmospheric Physics, Beijing, China

9        <sup>3</sup>Department of Atmospheric and Oceanic Science and Earth System Science Interdisciplinary  
10       Center, University of Maryland, College Park, Maryland, USA

11       <sup>4</sup>Joint Center for Data Assimilation Research and Applications/Key Laboratory of Meteorological  
12       Disaster of Ministry of Education, Nanjing University of Information Science & Technology,  
13       Nanjing, China

14       <sup>5</sup>Department of Geography, University of Toronto, Ontario M5S3G3, Canada

15       <sup>6</sup>College of Engineering, Mathematics and Physical Sciences, Unvernity of Exeter, Exeter EX4  
16       4QE, UK

17       <sup>7</sup>Department of Atmosheric Sciences, University of Illinois at Urbana-Champaign, Urbana, IL  
18       61801, USA

19       <sup>8</sup>Climate and Environmental Physics, Physics Institute, University of Bern, Bern, Switzerland

20       <sup>9</sup>Oeschger Centre for Climate Change Research, University of Bern, Bern, Switzerland

21       <sup>10</sup>Land in the Earth System, Max Planck Institute for Meteorology, D-20146 Hamburg, Germany

22       <sup>11</sup>College of Life and Environmental Sciences, University of Exeter EX4 4QF, UK

23       <sup>12</sup>Laboratoire des Sciences du Climat et de l'Environnement, LSCE/IPSL-CEA-CNRS-UVQS,  
24       F-91191, Gif sur Yvette, France

25       <sup>13</sup>Met office Hadley Centre, Fitzroy Rd, Exeter. EX1 3PB. UK

26  
27       **Correspondence to: (Ning Zeng, zeng@umd.edu; Fei Jiang, jiangf@nju.edu.cn)**

28

29 **Abstract**

30 El Niño has two different flavors, eastern Pacific (EP) and central Pacific (CP) El  
31 Niños, with different global teleconnections. However, their different impacts on the  
32 interannual carbon cycle variability remain unclear. We here compared the behaviors  
33 of interannual atmospheric CO<sub>2</sub> variability and analyzed their terrestrial mechanisms  
34 during these two types of El Niños, based on the Mauna Loa (MLO) CO<sub>2</sub> growth rate  
35 (CGR) and the Dynamic Global Vegetation Model's (DGVM) historical simulations.  
36 The composite analysis showed that evolution of the MLO CGR anomaly during EP  
37 and CP El Niños had three clear differences: (1) negative or neutral precursors in the  
38 boreal spring during an El Niño-developing year (denoted as "yr0"), (2) strong or  
39 weak amplitudes, and (3) durations of the peak from December (yr0) to April during  
40 an El Niño-decaying year (denoted as "yr1") compared to October (yr0) to January  
41 (yr1) for a CP El Niño, respectively. The global land-atmosphere carbon flux ( $F_{TA}$ )  
42 simulated by multi-models was able to capture the essentials of these characteristics.  
43 We further found that the gross primary productivity (GPP) over the tropics and the  
44 extratropical southern hemisphere (Trop+SH) generally dominated the global  $F_{TA}$   
45 variations during both El Niño types. Regional analysis showed that during EP El  
46 Niño events significant anomalous carbon uptake caused by increased precipitation  
47 and colder temperatures, corresponding to the negative precursor, occurred between  
48 30°S and 20°N from January (yr0) to June (yr0). The strongest anomalous carbon  
49 releases, largely due to the reduced GPP induced by low precipitation and warm  
50 temperatures, occurred between the equator and 20°N from February (yr1) to August  
51 (yr1). In contrast, during CP El Niño events, clear carbon releases existed between  
52 10°N and 20°S from September (yr0) to September (yr1), resulting from the  
53 widespread dry and warm climate conditions. Different spatial patterns of land

54 temperatures and precipitation in different seasons associated with EP and CP El  
55 Niños accounted for the evolutionary characteristics of GPP, terrestrial ecosystem  
56 respiration (TER), and the resultant  $F_{TA}$ . Understanding these different behaviors of  
57 interannual atmospheric CO<sub>2</sub> variability, along with their terrestrial mechanisms  
58 during EP and CP El Niños, is important because the CP El Niño occurrence rate  
59 might increase under global warming.

60

## 61 **1 Introduction**

62 The El Niño–Southern Oscillation (ENSO), a dominant year-to-year climate variation,  
63 leads to a significant interannual variability in the atmospheric CO<sub>2</sub> growth rate (CGR)  
64 (Bacastow, 1976; Keeling et al., 1995). Many studies, including measurement  
65 campaigns (Lee et al., 1998; Feely et al., 2002), atmospheric inversions (Bousquet et  
66 al., 2000; Peylin et al., 2013), and terrestrial carbon cycle models (Zeng et al., 2005;  
67 Wang et al., 2016), have consistently suggested the dominant role of terrestrial  
68 ecosystems, especially tropical ecosystems, in contributing to interannual atmospheric  
69 CO<sub>2</sub> variability. Recently, Ahlstrom et al. (2015) further suggested ecosystems over  
70 the semi-arid regions played the most important role in the interannual variability of  
71 the land CO<sub>2</sub> sink. Moreover, this ENSO-related interannual carbon cycle variability  
72 may be enhanced under global warming, with approximately a 44% increase in the  
73 sensitivity of terrestrial carbon flux to ENSO (Kim et al., 2017).

74 Tropical climatic variations (especially in surface air temperature and precipitation)  
75 induced by ENSO and plant and soil physiological responses can largely account for  
76 interannual terrestrial carbon cycle variability (Zeng et al., 2005; Wang et al., 2016;  
77 Jung et al., 2017). Multi-model simulations involved in the TRENDY project and the  
78 Coupled Model Intercomparison Project Phase 5 (CMIP5) have consistently

79 suggested the biological dominance of gross primary productivity (GPP) or net  
80 primary productivity (NPP) (Kim et al., 2016; Wang et al., 2016; Piao et al., 2013;  
81 Ahlstrom et al., 2015). However, debates continue regarding which is the dominant  
82 climatic mechanism (temperature or precipitation) in the interannual variability of the  
83 terrestrial carbon cycle (Wang et al., 2013; Wang et al., 2014; Cox et al., 2013; Zeng  
84 et al., 2005; Ahlstrom et al., 2015; Wang et al., 2016; Qian et al., 2008; Jung et al.,  
85 2017).

86 The atmospheric CGR or land-atmosphere carbon flux ( $F_{TA}$  – if this is positive, this  
87 indicates a flux into the atmosphere) can anomalously increase during El Niño, and  
88 decrease during La Niña episodes (Zeng et al., 2005; Keeling et al., 1995). Cross  
89 correlation analysis shows that atmospheric CGR and  $F_{TA}$  lags the ENSO by several  
90 months (Qian et al., 2008; Wang et al., 2013; Wang et al., 2016). This is due to the  
91 period needed for surface energy and soil moisture adjustment following  
92 ENSO-related circulation and precipitation anomalies (Gu and Adler, 2011; Qian et al.,  
93 2008). However, considering the variability inherent in the ENSO phenomenon  
94 (Capotondi et al., 2015), the atmospheric CGR and  $F_{TA}$  can show different behaviors  
95 during different El Niño events (Schwalm, 2011; Wang et al., 2018).

96 El Niño events can be classified into eastern Pacific El Niño (EP El Niño, also termed  
97 as conventional El Niño) and central Pacific El Niño (CP El Niño, also termed as El  
98 Niño Modoki) according to the patterns of sea-surface warming over the tropical  
99 Pacific (Ashok et al., 2007; Ashok and Yamagata, 2009). These two types of El Niño  
100 have different global climatic teleconnections, associated with contrasting climate  
101 conditions in different seasons (Weng et al., 2007; Weng et al., 2009). For example,  
102 positive winter temperature anomalies are located mostly over the northeastern US  
103 during an EP El Niño, while warm anomalies occur in the northwestern US during a

104 CP El Niño (Yu et al., 2012). The contrasting summer and winter precipitation  
105 anomaly patterns associated with these two El Niño events over the China, Japan, and  
106 the US were also discussed by Weng et al. (2007; 2009). Importantly, Ashok et al.  
107 (2007) suggested that the occurrence of the CP El Niño had increased during recent  
108 decades compared to the EP El Niño. This phenomenon can probably be attributed to  
109 the anthropogenic global warming (Ashok and Yamagata, 2009; Yeh et al., 2009).  
110 However, the contrasting impacts of EP and CP El Niño events on carbon cycle  
111 variability remain unclear. In this study, we attempt to reveal their different impacts  
112 given the different regional responses of the EP and CP El Niños. We compared the  
113 behavior of interannual atmospheric CO<sub>2</sub> variability and analyzed their terrestrial  
114 mechanisms corresponding to these two types of El Niños, based on Mauna Loa  
115 long-term CGR and TRENDY multi-model simulations.  
116 This paper is organized as follows: section 2 describes the datasets used, methods, and  
117 TRENDY models selected. Section 3 reports the results regarding the relationship  
118 between ENSO and CGR and EP and CP El Niño events, in addition to a composite  
119 analysis on carbon cycle behaviors, and terrestrial mechanisms. Section 4 contains a  
120 discussion of the results, and section 5 presents concluding remarks.

121

## 122 **2 Datasets and Methods**

### 123 **2.1 Datasets used**

124 Data for monthly atmospheric CO<sub>2</sub> concentrations between 1960 and 2013 was  
125 collected from the National Oceanic and Atmospheric Administration (NOAA) Earth  
126 System Research Laboratory (ESRL). The annual CO<sub>2</sub> growth rate (CGR) in Pg C  
127 yr<sup>-1</sup> was derived month by month according to the approach described by Patra et al.,

128 (2005) and Sarmiento et al. (2010). The calculation is as follows:

$$129 \quad CGR(t) = \gamma \cdot [pCO_2(t + 6) - pCO_2(t - 6)] \quad (1)$$

130 where  $\gamma = 2.1276 \text{ Pg C ppm}^{-1}$ ;  $pCO_2$  is the atmospheric partial pressure of  $CO_2$  in  
131 ppm; and  $t$  is the time in months. The detailed calculation of the conversion factor,  $\gamma$ ,  
132 can be found in the appendix (Sarmiento et al., 2010).

133 Temperature and precipitation datasets for 1960 through 2013 were obtained from  
134 CRUNCEPv6 (Wei et al., 2014). CRUNCEP datasets are the merged product of  
135 ground observation-based CRU data and model-based NCEP-NCAR Reanalysis data  
136 with a  $0.5^\circ \times 0.5^\circ$  spatial resolution and 6-hour temporal resolution. These datasets  
137 are consistent with the climatic forcing used to run dynamic global vegetation models  
138 in TRENDY v4 (Sitch et al., 2015). The sea surface temperature anomalies (SSTA)  
139 over the Niño3.4 region ( $5^\circ\text{S}$ – $5^\circ\text{N}$ ,  $120^\circ$ – $170^\circ\text{W}$ ) were obtained from the NOAA’s  
140 Extended Reconstructed Sea Surface Temperature (ERSST) dataset, version 4 (Huang  
141 et al., 2015).

142 The inversion of  $F_{TA}$  from the Jena CarboScope was used for comparison with the  
143 TRENDY multi-model simulations from 1981 to 2013. The Jena CarboScope Project  
144 provided the estimates of the surface-atmosphere carbon flux based on atmospheric  
145 measurements using an “atmospheric transport inversion”. The inversion run used  
146 here was s81\_v3.8 (Rodenbeck et al., 2003).

147

148

## 149 **2.2 TRENDY simulations**

150 We analyzed eight state-of-the-art dynamic global vegetation models from TRENDY  
151 v4 for the period 1960–2013: CLM4.5 (Oleson et al., 2013), ISAM (Jain et al., 2013),  
152 JSBACH (Reick et al., 2013), JULES (Clark et al., 2011), LPX-Bern (Keller et al.,  
153 2017), OCN (Zaehle and Friend, 2010), VEGAS (Zeng et al., 2005), and VISIT (Kato  
154 et al., 2013) (Table 1). Since LPX-Bern was excluded in the analysis of TRENDY v4,  
155 due to it not fulfilling the minimum performance requirement, the output over the  
156 same time period of a more recent, better performing, version (LPX-Bern v1.3) was  
157 used. These models were forced using a common set of climatic datasets  
158 (CRUNCEPv6), and followed the same experimental protocol. Models use different  
159 vegetation datasets or internally generated vegetation. The ‘S3’ run was used in this  
160 study, in which simulations forced by all the drivers including CO<sub>2</sub>, climate, land use,  
161 and land cover change (Sitch et al., 2015).

162 The simulated terrestrial variables (NBP, GPP, TER, soil moisture, and others) were  
163 interpolated into a consistent 0.5°×0.5° resolution using the first-order conservative  
164 remapping scheme (Jones, 1999) by Climate Data Operators (CDO):

$$165 \quad \overline{F}_k = \frac{1}{A_k} \int f dA \quad (2)$$

166 where  $\overline{F}_k$  denotes the area-averaged destination quantity;  $A_k$  is the area of cell  $k$ ;  
167 and  $f$  is the quantity in an old grid which has overlapping area with the destination  
168 grid. Then the median, 5%, and 95% percentiles of the multi-model simulations were  
169 calculated grid by grid to study the different effects of EP and CP El Niños on

170 terrestrial carbon cycle interannual variability.

171

### 172 **2.3 El Niño criterion and classification methods**

173 El Niño events are determined by the Oceanic Niño Index (ONI) [i.e. the running  
174 3-month mean SST anomaly over the Niño3.4 region] (Fig. 1a). This NOAA criterion  
175 is that El Niño events are defined as 5 consecutive overlapping 3-month periods at or  
176 above the +0.5° anomaly.

177 We classified El Niño events into EP or CP based on the consensus of three different  
178 identification methods directly adopted from a previous study (Yu et al., 2012). These  
179 identification methods included the El Niño Modoki Index (EMI) (Ashok et al., 2007),  
180 the EP/CP-index method (Kao and Yu, 2009), and the Niño method (Yeh et al., 2009).

181

### 182 **2.4 Anomaly calculation and composite analysis**

183 To calculate the anomalies, we first removed the long-term climatology for the period  
184 from 1960 to 2013 from all of the variables used here, both modelled and observed, in  
185 order to eliminate seasonal cycle. We then detrended them based on a linear  
186 regression, because (1) the trend in terrestrial carbon variables was mainly caused by  
187 long-term CO<sub>2</sub> fertilization and climate change, and (2) the trend in CGR primarily  
188 resulted from the anthropogenic emissions. We used these detrended monthly  
189 anomalies to investigate the impacts of El Niño events on the interannual carbon cycle  
190 variability.

191 More specifically, in terms of the composite analysis, we calculated the averages of  
192 the carbon flux anomaly (CGR,  $F_{TA}$  i.e.) during the selected EP and CP El Niño



193 events, respectively. We use the Bootstrap Methods (Mudelsee, 2010) to estimate the  
194 95% confidence intervals and the Student's *t*-test to estimate the significance levels  
195 in the composite analysis. An 80% significance level was selected, as per Weng et al.  
196 (2007), due to the limited number of EP El Niño events.

197

### 198 **3 Results**

#### 199 **3.1 The relationship between ENSO and interannual atmospheric CO<sub>2</sub>** 200 **variability**

201 The interannual atmospheric CO<sub>2</sub> variability closely coupled with ENSO (Fig. 1) with  
202 noticeable increases in CGR during El Niño and decreases during La Niña,  
203 respectively (Bacastow, 1976; Keeling and Revelle, 1985). The correlation coefficient  
204 between the MLO CGR and the Niño3.4 Index from 1960 to 2013 was 0.43 ( $p <$   
205 0.01). A regression analysis further indicated that a per unit increase in the Niño3.4  
206 Index can lead to a 0.60 Pg C yr<sup>-1</sup> increase in the MLO CGR.

207 The variation in the global F<sub>TA</sub> anomaly simulated by TRENDY models resembled the  
208 MLO CGR variation, with a correlation coefficient of 0.54 ( $p < 0.01$ ; Fig. 1b). This  
209 was close to the correlation coefficient of 0.61 ( $p < 0.01$ ; Fig. 1b) between the MLO  
210 CGR and the Jena CarboScope s81 for the time period from 1981 to 2013. This  
211 indicates that the terrestrial carbon cycle can largely explain the interannual  
212 atmospheric CO<sub>2</sub> variability, as suggested by previous studies (Bousquet et al., 2000;  
213 Zeng et al., 2005; Peylin et al., 2013; Wang et al., 2016). Moreover, the correlation  
214 coefficient of the TRENDY global F<sub>TA</sub> and the Niño3.4 Index reached 0.49 ( $p <$

215 0.01), and a similar regression analysis of  $F_{TA}$  with Niño3.4 showed a sensitivity of  
216  $0.64 \text{ Pg C yr}^{-1} \text{ K}^{-1}$ . However, owing to the diffuse light fertilization effect induced by  
217 the eruption of Mount Pinatubo in 1991 (Mercado et al., 2009), the Jena CarboScope  
218 s81 indicated that the terrestrial ecosystems had an anomalous uptake during the  
219 1991/92 El Niño event, making the MLO CGR an anomalous decrease. However,  
220 TRENDY models did not capture this phenomenon. This was not only due to a lack of  
221 a corresponding process representation in some models, but also because the  
222 TRENDY protocol did not include diffuse and direct light forcing.

223

### 224 **3.2 EP and CP El Niño events**

225 Schematic diagrams of the two types of El Niños (EP and CP) are shown in Fig. 2.  
226 During EP El Niño events (Fig. 2a), a positive sea surface temperature anomaly  
227 (SSTA) occurs in the eastern equatorial Pacific Ocean, showing a dipole SSTA pattern  
228 with the positive zonal SST gradient. This condition forms a single cell of Walker  
229 circulation over the tropical Pacific, with a dry downdraft in the western Pacific and  
230 wet updraft in the central-eastern Pacific. In contrast, an anomalous warming in the  
231 central Pacific, sandwiched by anomalous cooling in the east and west, is observed  
232 during CP El Niño events (Fig. 2b). This tripole SSTA pattern makes the  
233 positive/negative zonal SST gradient in the western/eastern tropical Pacific, resulting  
234 in an anomalous two-cell Walker circulation over the tropical Pacific. This alteration  
235 in atmospheric circulation produces a wet region in the central Pacific. Moreover,  
236 apart from these differences in the equatorial Pacific, the SSTA in other oceanic

237 regions also differ remarkably (Weng et al., 2007; Weng et al., 2009).  
238 Based on the NOAA criterion, a total of 17 El Niño events were detected from 1960  
239 through 2013. The events were then categorized into an EP or a CP El Niño based on  
240 a consensus of three identification methods (EMI, EP/CP-index, and Niño methods)  
241 (Yu et al., 2012). Considering the effect of diffuse radiation fertilization induced by  
242 volcano eruptions (Mercado et al., 2009), we removed the 1963/64, 1982/83, and  
243 1991/92 El Niño events, in which Mount Agung, El Chichón, and Pinatubo erupted,  
244 respectively. In addition, we closely examined those extended El Niño events that  
245 occurred in 1968/70, 1976/78, and 1986/88. Based on the typical responses of MLO  
246 CGR to El Niño events (anomalous increase lasting from the El Niño developing year  
247 to El Niño decaying year; Supplementary Fig. S1), we retained 1968/69, 1976/77, and  
248 1987/88 El Niño periods. Finally, we got 4 EP El Niño and 7 CP El Niño events in  
249 this study (Table 2; Fig. 1b and Supplementary Fig. S2), with the composite SSTA  
250 evolutions as shown in Supplementary Fig. S3.

251

### 252 **3.3 Responses of atmospheric CGR to two types of El Niños**

253 Based on the selected EP and CP El Niño events, a composite analysis was conducted  
254 with the non-smoothed detrended monthly anomalies of the MLO CGR and the  
255 TRENDY global  $F_{TA}$  to reveal the contrasting carbon cycle responses to these two  
256 types of El Niños (Fig. 3). In addition to the differences in the location of anomalous  
257 SST warming and the alteration of the atmospheric circulation in EP and CP El Niños  
258 shown in Fig. 2, the following findings were elucidated: (1) different El Niño

259 precursors: the SSTA was significantly negative in EP El Niño during the boreal  
260 winter (JF) and spring (MAM) in yr0 (hereafter yr0 and yr1 refer to the El Niño  
261 developing and decaying year, respectively). Conversely, the SSTA was neutral in CP  
262 El Niño; (2) different tendencies of SST ( $\partial SSTA/\partial t$ ): the tendency of SST in EP El  
263 Niño was stronger than that in CP El Niño; (3) different El Niño amplitudes: due to  
264 the different tendencies of SST, the amplitude of EP El Niño was basically stronger  
265 than that of CP El Niño, though they all reached maturity in November or December  
266 of yr0 (Figs. 3a and 3c).

267 Correspondingly, behaviors of the MLO CGR during these two types of El Niño  
268 events also displayed some differences (Figs. 3b and 3d). During EP El Niño events  
269 (Fig. 3b), the MLO CGR was negative in boreal spring (yr0) and increased quickly  
270 from boreal fall (yr0), whereas it was neutral in boreal spring (yr0) and slowly  
271 increases from boreal summer (yr0) during the CP El Niño episode (Fig. 3d). The  
272 amplitude of the MLO CGR anomaly during EP El Niño events was generally larger  
273 than that during CP El Niño events. Importantly, the duration of the MLO CGR peak  
274 during EP El Niño was from December (yr0) to April (yr1), while the MLO CGR  
275 anomaly peaked from October (yr0) to January (yr1) during CP El Niño. We here  
276 simply defined the peak duration as the period above the 75% of the maximum CGR  
277 (or  $F_{TA}$ ) anomaly, in which the variabilities of less than 3 months below the threshold  
278 were also included. The positive MLO CGR anomaly ended around September (yr1)  
279 in both cases (Figs. 3b and 3d). During the finalization of this paper, we noted the

280 publication of Chylek et al. (2018) who also found CGR amplitude difference in  
281 response to the two types of events.

282 A comparison of the MLO CGR with the TRENDY global  $F_{TA}$  anomalies (Figs. 3b  
283 and 3d) indicated that the TRENDY global  $F_{TA}$  effectively captured the characteristics  
284 of CGR evolution during the CP El Niño. In contrast, the amplitude of the TRENDY  
285 global  $F_{TA}$  anomaly was somewhat underestimated during the EP El Niño, causing a  
286 lower statistical significance (Fig. 3b). This underestimation of the global  $F_{TA}$   
287 anomaly can, for example, be clearly seen in a comparison between the TRENDY and  
288 the Jena CarboScope during the extreme 1997/98 EP El Niño (Fig. 1b). Also, other  
289 characteristics can be basically captured. Therefore, insight into the mechanisms of  
290 these CGR evolutions during EP and CP El Niños, based on the simulations by  
291 TRENDY models, is still possible.

292

### 293 **3.4 Regional contributions, characteristics, and their mechanisms**

294 We separated the TRENDY global  $F_{TA}$  anomaly by major geographic regions into two  
295 parts: the extratropical northern hemisphere (NH, 23°N–90°N), and the tropics plus  
296 extratropical southern hemisphere (Trop+SH, 60°S–23°N) (Fig. 4). In a comparison of  
297 the contributions from these two parts, it was found that the  $F_{TA}$  over Trop+SH played  
298 a more important role in the global  $F_{TA}$  anomaly in both cases (Figs. 4b and 4d), and  
299 this finding was consistent with previous studies (Bousquet et al., 2000; Peylin et al.,  
300 2013; Zeng et al., 2005; Wang et al., 2016; Ahlstrom et al., 2015; Jung et al., 2017).

301 The  $F_{TA}$  over Trop+SH was negative in austral fall (MAM; yr0), increased from

302 austral spring (SON; yr0), and peaked from December (yr0) to April (yr1) during the  
303 EP El Niño (Fig. 4b). Conversely, it was nearly neutral in austral fall (yr0), increased  
304 from austral winter (JJA; yr0), and peaked from November (yr0) to March (yr1)  
305 during the CP El Niño (Fig. 4d). These evolutionary characteristics in the  $F_{TA}$  over the  
306 Trop+SH were generally consistent with the global  $F_{TA}$  and the MLO CGR (Figs. 3b  
307 and 3d). In contrast, the contributions from the  $F_{TA}$  anomaly over the NH were  
308 relatively weaker (or nearly neutral) (Figs. 4a and 4c).

309 According to the equation  $F_{TA} = -NBP = TER - GPP + D$  (where  $D$  is the carbon  
310 flux caused by the disturbances such as the wildfires, harvests, grazing, land cover  
311 change etc.), the variation in  $F_{TA}$  can be explained by the variations in GPP, TER, and  
312  $D$ . The  $D$  simulated by TRENDY was nearly neutral during both El Niño types (Fig.  
313 4). Therefore, GPP and TER largely accounted for the variation in  $F_{TA}$ .

314 More Specifically, in Trop+SH, GPP anomalies dominated the variations in  $F_{TA}$  for  
315 both El Niño types, but their evolutions differed (Figs. 4b and 4d). The GPP showed  
316 an anomalous positive value during austral fall (yr0), and an anomalous negative  
317 value from austral fall (yr1) to winter (yr1), with the minimum around April (yr1)  
318 during the EP El Niño (Fig. 4b). Conversely, the GPP anomaly was always negative,  
319 with the minimum occurring around October or November (yr0) during the CP El  
320 Niño (Fig. 4d). The variation in the TER in both El Niños was relatively weaker than  
321 that of the GPP (Figs. 4b and d). The anomalous positive TER during austral spring  
322 (yr0) and summer (yr1) accounted for the increase in  $F_{TA}$ , and it partly canceled the

323 negative GPP in austral fall (yr1) and winter (yr1) during the EP El Niño (Fig. 4b). In  
324 contrast, the TER had a reduction in yr0 during the CP El Niño (Fig. 4d). Over the  
325 NH, though the  $F_{TA}$  anomaly was relatively weaker, the behaviors of GPP and TER  
326 differed in EP and CP El Niños. GPP and TER consistently decreased in the growing  
327 season of yr0 and increased in the growing season of yr1 during the EP El Niño (Fig.  
328 4a), whereas they only showed some increase during boreal summer (yr1) during the  
329 CP El Niño (Fig. 4c).

330 These evolutionary characteristics of GPP, TER, and the resultant  $F_{TA}$  principally  
331 resulted from their responses to the climate variability. Figure 5 shows the  
332 standardized observed surface air temperature, precipitation, and TRENDY simulated  
333 soil moisture contents. Over the Trop+SH, taking into consideration the regulation of  
334 thermodynamics and hydrological cycle on surface energy balance, variations in  
335 temperature and precipitation (soil moisture) were always opposite during the two  
336 types of El Niños (Figs. 5b and d). Additionally, adjustments in soil moisture lagged  
337 precipitation by approximately 2–4 months, owing to the so-called ‘soil memory’ of  
338 water recharge (Qian et al., 2008). The variations in GPP in both the El Niño types  
339 were closely associated with variations in soil moisture, namely water availability  
340 largely dominated by precipitation (Figs. 4b and 4d and 5b and 5d), and this result  
341 was consistent with previous studies (Zeng et al., 2005; Zhang et al., 2016). Warm  
342 temperatures during El Niño episodes can enhance the ecosystem respiration, but dry  
343 conditions can reduce it. These cancellations from warm and dry conditions made the

344 amplitude of TER variation smaller than that of GPP (Figs. 4b and 4d). Over the NH,  
345 variations in temperature and precipitation were basically in the same direction (Figs.  
346 5a and 5c), as opposed to their behaviors over the Trop+SH. This was due to the  
347 different climatic dynamics of the two regions (Zeng et al., 2005). During the EP El  
348 Niño event, cool and dry conditions in the boreal summer (yr0) inhibited GPP and  
349 TER, whereas warm and wet conditions in the boreal spring and summer (yr1)  
350 enhanced them (Figs. 5a and 4a). In contrast, only the warm and wet conditions in  
351 boreal summer (yr1) enhanced GPP and TER during the CP El Niño event. (Figs. 5c  
352 and 4c). These different configurations of temperature and precipitation variations  
353 during EP and CP El Niños form the different evolutionary characteristics of GPP,  
354 TER, and the resultant  $F_{TA}$ .

355 Detailed regional evolutionary characteristics can be seen from the Hovmöller  
356 diagrams in Fig. 6 and in Supplementary Figs. S4 and S5. Obvious large anomalies in  
357  $F_{TA}$  consistently occurred from 20°N to 40°S during EP and CP El Niños (Figs. 6c and  
358 6f), consistent with the above analyses (Figs. 4b and 4d). Moreover, there was a clear  
359 anomalous carbon uptake between 30°S and 20°N during the period from January  
360 (yr0) to June (yr0) during the EP El Niño (Fig. 6c). This uptake corresponded to the  
361 negative precursor (Figs. 3b and 4b). This anomalous carbon uptake comparably came  
362 from the three continents (Supplementary Figs. S4 a–c). Biological process analyses  
363 indicated that GPP dominated between 5°N and 20°N, and between 30°S and 15°S  
364 (Supplementary Fig. S5a), which was related to the increased amount of precipitation



365 (Fig. 6b). In contrast, TER dominated between 15°S and 5°N (Supplementary Fig.  
366 S5b), largely due to the colder temperatures (Fig. 6a). Conversely, the strongest  
367 anomalous carbon releases occurred between the equator and 20°N during the period  
368 from February (yr1) to August (yr1) during the EP El Niño (Fig. 6c). The largest  
369 contribution to these anomalous carbon releases came from the South America  
370 (Supplementary Fig. S4c). Both GPP and TER showed the anomalous decreases  
371 (Supplementary Figs. S5a and S5b), and stronger decrease in GPP than in TER made  
372 the anomalous carbon releases here (Fig. 6c). Low precipitation (with a few months of  
373 delayed dry conditions; Fig. 6b) and warm temperatures (Fig. 6a) inhibited GPP,  
374 causing the positive  $F_{TA}$  anomaly (Fig. 6c). In contrast, significant carbon releases  
375 were found between 10°N and 20°S from September (yr0) to September (yr1) during  
376 the CP El Niño (Fig. 6f). More specifically, these clear carbon releases largely  
377 originated from South America and tropical Asia (Supplementary Figs. S4 d–f). TER  
378 dominated between 15°S and 10°N during the period from January (yr1) to September  
379 (yr1), and other regions and periods were dominated by GPP (Supplementary Figs.  
380 S5c and S5d). Widespread dry and warm conditions (Figs. 6d and e) effectively  
381 explained these GPP and TER anomalies, as well as the resultant  $F_{TA}$  behavior. For  
382 more detailed information on the other regions, refer to Supplementary Figs. S4 and  
383 S5.

384

#### 385 **4 Discussion**

386 El Niño shows large diversity in individual events (Capotondi et al., 2015), thereby

387 creating large uncertainties in composite analyses (Figs. 3–5). Four EP El Niño events  
388 during the past five decades were selected for this study to research their effects on  
389 interannual carbon cycle variability (Table 1). Due to the small number of samples  
390 and large inter-event spread (Supplementary Fig. S2), the statistical significance of  
391 the composite analyses will need to be further evaluated with upcoming EP El Niño  
392 events occurring in the future. However, cross-correlation analyses between the  
393 long-term CGR (or  $F_{TA}$ ) and the Niño Index have shown that the responses of CGR  
394 (or  $F_{TA}$ ) lag ENSO by a few months (Zeng et al., 2005; Wang et al., 2016; Wang et al.,  
395 2013). This phenomenon can be clearly detected in the EP El Niño composite (Fig.  
396 3b). Therefore, the composite analyses in this study can still give us some insight into  
397 the interannual variability of the global carbon cycle.

398 Another caveat is that the TRENDY models seemed to underestimate the amplitude of  
399 the  $F_{TA}$  anomaly during the extreme EP El Niño events (Fig. 1b). This  
400 underestimation of  $F_{TA}$  may partially result from a bias in the estimation of carbon  
401 releases induced by wildfires. As expected, the carbon releases induced by wildfires  
402 in such 1997/98 strong El Niño event played an important role in global carbon  
403 variations (van der Werf et al., 2004; Chen et al., 2017) (Supplementary Fig. S6).  
404 However, some TRENDY models (ISAM, JULES, and OCN) do not include a fire  
405 module to explicitly simulate the carbon releases induced by wildfires (Table 1), and  
406 those TRENDY models that do contain a fire module generally underestimate the  
407 effects of wildfires. For instance, VISIT and JSBACH clearly underestimated the

408 carbon flux anomaly induced by wildfires during the 1997/98 EP El Niño event  
409 (Supplementary Fig. S6).

410 The recent extreme 2015/16 El Niño event was not included in this study, because the  
411 TRENDY v4 datasets covered the time span from 1860 to 2014. As shown in Wang et  
412 al. (2018), the behavior of the MLO CGR in the 2015/16 El Niño resembled the  
413 composite result of the CP El Niño events (Fig. 3d). But the 2015/16 El Niño event  
414 had the extreme positive SSTA both over the central and eastern Pacific. Its equatorial  
415 eastern Pacific SSTA exceeded +2.0 K, comparable to the historical extreme El Niño  
416 events (e.g. 1982/83, 1997/98); the central Pacific SSTA marked the warmest event  
417 since the modern observation (Thomalla and Boyland, 2017). Therefore, the 2015/16  
418 El Niño event evolved not only in a similar fashion to the EP El Niño dynamics that  
419 rely on the basin-wide thermocline variations, but also in a similar fashion to the CP  
420 El Niño dynamics that rely on the subtropical forcing (Paek et al., 2017; Palmeiro et  
421 al., 2017). The 2015/16 extreme El Niño event can be treated as the strongest mixed  
422 EP and CP El Niño that caused different climate anomalies compared with the  
423 extreme 1997/98 El Niño (Paek et al., 2017; Palmeiro et al., 2017), which had  
424 contrasting terrestrial and oceanic carbon cycle responses (Wang et al., 2018; Liu et  
425 al., 2017; Chatterjee et al., 2017).

426 As above mentioned, when finalizing our paper, we noted the publication of Chylek et  
427 al. (2018) who also focused on interannual atmospheric CO<sub>2</sub> variability during EP and  
428 CP El Niño events. We here simply illustrated some differences and similarities. In

429 the method of the identification of EP and CP El Niño events, Chylek et al. (2018)  
430 took the Niño1+2 index and Niño4 index to categorize El Niño events, while we  
431 adopted the results of Yu et al. (2012), based on the consensus of three different  
432 identification methods, and additionally excluded the events that coincided with  
433 volcanic eruptions. The different methods made some differences in the identification  
434 of EP and CP El Niño events. Chylek et al. (2018) suggested that the CO<sub>2</sub> rise rate had  
435 different time delay to the tropical near surface air temperature, with the delay of  
436 about 8.5 and 4 months during EP and CP El Niños, respectively. Although we did not  
437 find out the exactly same time delay, we suggested that MLO CGR anomaly showed  
438 the peak duration from December (yr0) to April (yr1) in EP El Niños, and from  
439 October (yr0) to January (yr1) in CP El Niños. Additionally, we suggested the  
440 differences of MLO CGR anomaly in precursors and amplitudes during EP and CP El  
441 Niños. Furthermore, we revealed their terrestrial mechanisms based on the inversion  
442 results and the TRENDY multi-model historical simulations.

443

## 444 **5 Concluding Remarks**

445 In this study, we investigate the different impacts of EP and CP El Niño events on the  
446 interannual carbon cycle variability in terms of the composite analysis, based on the  
447 long-term MLO CGR and TRENDY multi-model simulations. We suggest that there  
448 are three clear differences in evolutions of the MLO CGR during EP and CP El Niños  
449 in terms of their precursor, amplitude, and duration of the peak. Specifically, the MLO

450 CGR anomaly was negative in boreal spring (yr0) during EP El Niño events, while it  
451 was neutral during CP El Niño events. Additionally, the amplitude of the CGR  
452 anomaly was generally larger during EP El Niño events than during CP El Niño  
453 events. Also, the duration of the MLO CGR peak during EP El Niño events occurred  
454 from December (yr0) to April (yr1), while it peaked from October (yr0) to January  
455 (yr1) during CP El Niño events.

456 The TRENDY multi-model simulated global  $F_{TA}$  anomalies were able to capture these  
457 characteristics. Further analysis indicated that the  $F_{TA}$  anomalies over the Trop+SH  
458 made the largest contribution to the global  $F_{TA}$  anomalies during these two types of El  
459 Niño events, in which GPP anomalies, rather than TER anomalies, generally  
460 dominated the evolutions of the  $F_{TA}$  anomalies. Regionally, during EP El Niño events,  
461 clear anomalous carbon uptake occurred between 30°S and 20°N during the period  
462 from January (yr0) to June (yr0), corresponding to the negative precursor. This was  
463 primarily caused by more precipitation and colder temperatures. The strongest  
464 anomalous carbon releases happened between the equator and 20°N during the period  
465 from February (yr1) to August (yr1), largely due to the reduced GPP induced by low  
466 precipitation and warm temperatures. In contrast, clear carbon releases existed  
467 between 10°N and 20°S from September (yr0) to September (yr1) during CP El Niño  
468 events, which were caused by widespread dry and warm climate conditions.

469 Some studies (Yeh et al., 2009; Ashok and Yamagata, 2009) have suggested that the  
470 CP El Niño has become or will be more frequent under global warming compared

471 with the EP El Niño. Because of these different behaviors of the interannual carbon  
472 cycle variability during the two types of El Niños, this shift of El Niño types will alter  
473 the response patterns of interannual terrestrial carbon cycle variability. This  
474 possibility should encourage researchers to perform further studies in the future.

475

476 **Data availability.** The monthly atmospheric CO<sub>2</sub> concentration is from NOAA/ESRL  
477 (<https://www.esrl.noaa.gov/gmd/ccgg/trends/index.html>). The Niño3.4 Index is from  
478 ERSST4 (<http://www.cpc.ncep.noaa.gov/data/indices/ersst4.nino.mth.81-10.ascii>).  
479 Temperature and precipitation are from CRUNCEP v6  
480 ([ftp://nacp.ornl.gov/synthesis/2009/frescati/temp/land\\_use\\_change/original/readme.ht](ftp://nacp.ornl.gov/synthesis/2009/frescati/temp/land_use_change/original/readme.htm)  
481 [m](ftp://nacp.ornl.gov/synthesis/2009/frescati/temp/land_use_change/original/readme.htm)). TRENDY v4 data are available from S. Sitch ([s.a.sitch@exeter.ac.uk](mailto:s.a.sitch@exeter.ac.uk)) upon your  
482 reasonable request.

483

484 **Acknowledgements.** We gratefully acknowledge the TRENDY DGVM community,  
485 as part of the Global Carbon Project, for access to gridded land data and the NOAA  
486 ESRL for the use of Mauna Loa atmospheric CO<sub>2</sub> records. This study was supported  
487 by the National Key R&D Program of China (grant no. 2016YFA0600204 and no.  
488 2017YFB0504000), the Natural Science Foundation of Jiangsu Province, China  
489 (Grant No. BK20160625), and the National Natural Science Foundation of China  
490 (Grant No. 41605039). Andrew Wiltshire was supported by the Joint UK BEIS/Defra  
491 Met Office Hadley Centre Climate Programme (GA01101). We also would like to

492 thank LetPub for proving linguistic assistance.

493

494 **References**

- 495 Ahlstrom, A., Raupach, M. R., Schurgers, G., Smith, B., Arneeth, A., Jung, M.,  
496 Reichstein, M., Canadell, J. G., Friedlingstein, P., Jain, A. K., Kato, E., Poulter,  
497 B., Sitch, S., Stocker, B. D., Viovy, N., Wang, Y. P., Wiltshire, A., Zaehle, S., and  
498 Zeng, N.: The dominant role of semi-arid ecosystems in the trend and variability  
499 of the land CO<sub>2</sub> sink, *Science*, 348, 895-899, 10.1126/science.aaa1668, 2015.
- 500 Ashok, K., Behera, S. K., Rao, S. A., Weng, H., and Yamagata, T.: El Niño Modoki  
501 and its possible teleconnection, *Journal of Geophysical Research*, 112,  
502 10.1029/2006jc003798, 2007.
- 503 Ashok, K., and Yamagata, T.: CLIMATE CHANGE The El Nino with a difference,  
504 *Nature*, 461, 481-+, 10.1038/461481a, 2009.
- 505 Bacastow, R. B.: Modulation of atmospheric carbon dioxide by the Southern  
506 Oscillation, *Nature*, 261, 116-118, doi:10.1038/261116a0, 1976.
- 507 Bousquet, P., Peylin, P., Ciais, P., Le Quere, C., Friedlingstein, P., and Tans, P. P.:  
508 Regional changes in carbon dioxide fluxes of land and oceans since 1980,  
509 *Science*, 290, 1342-1346, Doi 10.1126/Science.290.5495.1342, 2000.
- 510 Capotondi, A., Wittenberg, A. T., Newman, M., Di Lorenzo, E., Yu, J.-Y., Braconnot,  
511 P., Cole, J., Dewitte, B., Giese, B., Guilyardi, E., Jin, F.-F., Karnauskas, K.,  
512 Kirtman, B., Lee, T., Schneider, N., Xue, Y., and Yeh, S.-W.: Understanding  
513 ENSO Diversity, *B Am Meteorol Soc*, 96, 921-938, 10.1175/bams-d-13-00117.1,

514 2015.

515 Chatterjee, A., Gierach, M. M., Sutton, A. J., Feely, R. A., Crisp, D., Eldering, A.,  
516 Gunson, M. R., O'Dell, C. W., Stephens, B. B., and Schimel, D. S.: Influence of  
517 El Nino on atmospheric CO<sub>2</sub> over the tropical Pacific Ocean: Findings from  
518 NASA's OCO-2 mission, *Science*, 358, 10.1126/science.aam5776, 2017.

519 Chen, Y., Morton, D. C., Andela, N., van der Werf, G. R., Giglio, L., and Randerson, J.  
520 T.: A pan-tropical cascade of fire driven by El Niño/Southern Oscillation, *Nature*  
521 *Climate Change*, 7, 906-911, 10.1038/s41558-017-0014-8, 2017.

522 Chylek, P., Tans, P., Christy, J., and Dubey, M. K.: The carbon cycle response to two  
523 El Nino types: an observational study, *Environmental Research Letters*, 13,  
524 10.1088/1748-9326/aa9c5b, 2018.

525 Clark, D. B., Mercado, L. M., Sitch, S., Jones, C. D., Gedney, N., Best, M. J., Pryor,  
526 M., Rooney, G. G., Essery, R. L. H., Blyth, E., Boucher, O., Harding, R. J.,  
527 Huntingford, C., and Cox, P. M.: The Joint UK Land Environment Simulator  
528 (JULES), model description - Part 2: Carbon fluxes and vegetation dynamics,  
529 *Geosci Model Dev*, 4, 701-722, 10.5194/gmd-4-701-2011, 2011.

530 Cox, P. M., Pearson, D., Booth, B. B., Friedlingstein, P., Huntingford, C., Jones, C. D.,  
531 and Luke, C. M.: Sensitivity of tropical carbon to climate change constrained by  
532 carbon dioxide variability, *Nature*, 494, 341-344, 10.1038/nature11882, 2013.

533 Feely, R. A., Boutin, J., Cosca, C. E., Dandonneau, Y., Etcheto, J., Inoue, H. Y., Ishii,  
534 M., Le Quere, C., Mackey, D. J., McPhaden, M., Metzl, N., Poisson, A., and



535 Wanninkhof, R.: Seasonal and interannual variability of CO<sub>2</sub> in the equatorial  
536 Pacific, *Deep-Sea Res Pt II*, 49, 2443-2469, Pii S0967-0645(02)00044-9, Doi  
537 10.1016/S0967-0645(02)00044-9, 2002.

538 Gu, G. J., and Adler, R. F.: Precipitation and Temperature Variations on the  
539 Interannual Time Scale: Assessing the Impact of ENSO and Volcanic Eruptions,  
540 *Journal of Climate*, 24, 2258-2270, Doi 10.1175/2010jcli3727.1, 2011.

541 Huang, B., Banzon, V. F., Freeman, E., Lawrimore, J., Liu, W., Peterson, T. C., Smith,  
542 T. M., Thorne, P. W., Woodruff, S. D., and Zhang, H.-M.: Extended  
543 Reconstructed Sea Surface Temperature Version 4 (ERSST.v4). Part I: Upgrades  
544 and Intercomparisons, *Journal of Climate*, 28, 911-930,  
545 10.1175/jcli-d-14-00006.1, 2015.

546 Jain, A. K., Meiyappan, P., Song, Y., and House, J. I.: CO<sub>2</sub> emissions from land-use  
547 change affected more by nitrogen cycle, than by the choice of land-cover data,  
548 *Global Change Biology*, 19, 2893-2906, 10.1111/gcb.12207, 2013.

549 Jones, P. W.: First- and second-order conservative remapping schemes for grids in  
550 spherical coordinates, *Mon Weather Rev*, 127, 2204-2210, Doi  
551 10.1175/1520-0493(1999)127<2204:Fasocr>2.0.Co;2, 1999.

552 Jung, M., Reichstein, M., Schwalm, C. R., Huntingford, C., Sitch, S., Ahlstrom, A.,  
553 Arneeth, A., Camps-Valls, G., Ciais, P., Friedlingstein, P., Gans, F., Ichii, K., Jain,  
554 A. K., Kato, E., Papale, D., Poulter, B., Raduly, B., Rodenbeck, C., Tramontana,  
555 G., Viovy, N., Wang, Y. P., Weber, U., Zaehle, S., and Zeng, N.: Compensatory

556 water effects link yearly global land CO<sub>2</sub> sink changes to temperature, *Nature*,  
557 541, 516-520, 10.1038/nature20780, 2017.

558 Kao, H.-Y., and Yu, J.-Y.: Contrasting Eastern-Pacific and Central-Pacific Types of  
559 ENSO, *Journal of Climate*, 22, 615-632, 10.1175/2008jcli2309.1, 2009.

560 Kato, E., Kinoshita, T., Ito, A., Kawamiya, M., and Yamagata, Y.: Evaluation of  
561 spatially explicit emission scenario of land-use change and biomass burning  
562 using a process-based biogeochemical model, *Journal of Land Use Science*, 8,  
563 104-122, 10.1080/1747423x.2011.628705, 2013.

564 Keeling, C. D., and Revelle, R.: Effects of El-Nino Southern Oscillation on the  
565 Atmospheric Content of Carbon-Dioxide, *Meteoritics*, 20, 437-450, 1985.

566 Keeling, C. D., Whorf, T. P., Wahlen, M., and Vanderpligt, J.: Interannual Extremes  
567 in the Rate of Rise of Atmospheric Carbon-Dioxide since 1980, *Nature*, 375,  
568 666-670, Doi 10.1038/375666a0, 1995.

569 Keller, K. M., Lienert, S., Bozbiyik, A., Stocker, T. F., Churakova, O. V., Frank, D. C.,  
570 Klesse, S., Koven, C. D., Leuenberger, M., Riley, W. J., Saurer, M., Siegwolf, R.,  
571 Weigt, R. B., and Joos, F.: 20th century changes in carbon isotopes and water-use  
572 efficiency: tree-ring-based evaluation of the CLM4.5 and LPX-Bern models,  
573 *Biogeosciences*, 14, 2641-2673, 10.5194/bg-14-2641-2017, 2017.

574 Kim, J.-S., Kug, J.-S., Yoon, J.-H., and Jeong, S.-J.: Increased Atmospheric CO<sub>2</sub>  
575 Growth Rate during El Niño Driven by Reduced Terrestrial Productivity in the  
576 CMIP5 ESMs, *Journal of Climate*, 29, 8783-8805, 10.1175/jcli-d-14-00672.1,

577 2016.

578 Kim, J.-S., Kug, J.-S., and Jeong, S.-J.: Intensification of terrestrial carbon cycle  
579 related to El Niño–Southern Oscillation under greenhouse warming, *Nature*  
580 *Communications*, 8, 10.1038/s41467-017-01831-7, 2017.

581 Lee, K., Wanninkhof, R., Takahashi, T., Doney, S. C., and Feely, R. A.: Low  
582 interannual variability in recent oceanic uptake of atmospheric carbon dioxide,  
583 *Nature*, 396, 155-159, Doi 10.1038/24139, 1998.

584 Liu, J., Bowman, K. W., Schimel, D. S., Parazoo, N. C., Jiang, Z., Lee, M., Bloom, A.  
585 A., Wunch, D., Frankenberg, C., Sun, Y., O'Dell, C. W., Gurney, K. R.,  
586 Menemenlis, D., Gierach, M., Crisp, D., and Eldering, A.: Contrasting carbon  
587 cycle responses of the tropical continents to the 2015-2016 El Nino, *Science*, 358,  
588 10.1126/science.aam5690, 2017.

589 Mercado, L. M., Bellouin, N., Sitch, S., Boucher, O., Huntingford, C., Wild, M., and  
590 Cox, P. M.: Impact of changes in diffuse radiation on the global land carbon sink,  
591 *Nature*, 458, 1014-U1087, Doi 10.1038/Nature07949, 2009.

592 Mudelsee, M.: *Climate Time Series Analysis: Classical Statistical and Bootstrap*  
593 *Methods*, Springer, Dordrecht, 2010.

594 Oleson, K., Lawrence, D., Bonan, G., Drewniak, B., Huang, M., Koven, C., Levis, S.,  
595 Li, F., Riley, W., Subin, Z., Swenson, S. C., Thorne, P. W., Bozbiyik, A., Fisher,  
596 R., Heald, C., Kluzek, E., Lamarque, J. F., Lawrence, P. J., Leung, L. R.,  
597 Lipscomb, W. H., Muszala, S., Ricciuto, D. M., Sacks, W. J., Tang, J., and Yang,

598 Z.: Technical Description of version 4.5 of the Community Land Model (CLM),  
599 NCAR, 2013.

600 Paek, H., Yu, J.-Y., and Qian, C.: Why were the 2015/2016 and 1997/1998 extreme El  
601 Niño different?, *Geophys Res Lett*, 44, 10.1002/2016GL071515, 2017.

602 Palmeiro, F. M., Iza, M., Barriopedro, D., Calvo, N., and García-Herrera, R.: The  
603 complex behavior of El Niño winter 2015-2016, *Geophys Res Lett*, 44,  
604 2902-2910, 10.1002/2017gl072920, 2017.

605 Patra, P. K., Maksyutov, S., Ishizawa, M., Nakazawa, T., Takahashi, T., and Ukita, J.:  
606 Interannual and decadal changes in the sea-air CO<sub>2</sub> flux from atmospheric CO<sub>2</sub>  
607 inverse modeling, *Global Biogeochemical Cycles*, 19, Artn Gb4013, Doi  
608 10.1029/2004gb002257, 2005.

609 Peylin, P., Law, R. M., Gurney, K. R., Chevallier, F., Jacobson, A. R., Maki, T., Niwa,  
610 Y., Patra, P. K., Peters, W., Rayner, P. J., Rödenbeck, C., van der Laan-Luijkx, I.  
611 T., and Zhang, X.: Global atmospheric carbon budget: results from an ensemble  
612 of atmospheric CO<sub>2</sub> inversions, *Biogeosciences*, 10, 6699-6720,  
613 10.5194/bg-10-6699-2013, 2013.

614 Piao, S., Sitch, S., Ciais, P., Friedlingstein, P., Peylin, P., Wang, X., Ahlström, A.,  
615 Anav, A., Canadell, J. G., Cong, N., Huntingford, C., Jung, M., Levis, S., Levy, P.  
616 E., Li, J., Lin, X., Lomas, M. R., Lu, M., Luo, Y., Ma, Y., Myneni, R. B., Poulter,  
617 B., Sun, Z., Wang, T., Viovy, N., Zaehle, S., and Zeng, N.: Evaluation of  
618 terrestrial carbon cycle models for their response to climate variability and to

619 CO<sub>2</sub> trends, *Global Change Biology*, 2117–2132, 10.1111/gcb.12187, 2013.

620 Qian, H., Joseph, R., and Zeng, N.: Response of the terrestrial carbon cycle to the El  
621 Nino-Southern Oscillation, *Tellus Series B-Chemical and Physical Meteorology*,  
622 60, 537-550, Doi 10.1111/J.1600-0889.2008.00360.X, 2008.

623 Reick, C. H., Raddatz, T., Brovkin, V., and Gayler, V.: Representation of natural and  
624 anthropogenic land cover change in MPI-ESM, *J Adv Model Earth Sy*, 5,  
625 459-482, 10.1002/jame.20022, 2013.

626 Rodenbeck, C., Houweling, S., Gloor, M., and Heimann, M.: CO<sub>2</sub> flux history  
627 1982-2001 inferred from atmospheric data using a global inversion of  
628 atmospheric transport, *Atmos. Chem. Phys.*, 3, 1919-1964,  
629 10.5194/acp-3-1919-2003, 2003.

630 Sarmiento, J. L., Gloor, M., Gruber, N., Beaulieu, C., Jacobson, A. R., Fletcher, S. E.  
631 M., Pacala, S., and Rodgers, K.: Trends and regional distributions of land and  
632 ocean carbon sinks, *Biogeosciences*, 7, 2351-2367, 2010.

633 Schwalm, C. R.: Does terrestrial drought explain global CO<sub>2</sub> flux anomalies induced  
634 by El Nino?, *Biogeosciences*, 8, 2493-2506, 2011.

635 Sitch, S., Friedlingstein, P., Gruber, N., Jones, S. D., Murray-Tortarolo, G., Ahlström,  
636 A., Doney, S. C., Graven, H., Heinze, C., Huntingford, C., Levis, S., Levy, P. E.,  
637 Lomas, M., Poulter, B., Viovy, N., Zaehle, S., Zeng, N., Arneeth, A., Bonan, G.,  
638 Bopp, L., Canadell, J. G., Chevallier, F., Ciais, P., Ellis, R., Gloor, M., Peylin, P.,  
639 Piao, S. L., Le Quéré, C., Smith, B., Zhu, Z., and Myneni, R.: Recent trends and

640 drivers of regional sources and sinks of carbon dioxide, *Biogeosciences*, 12,  
641 653-679, 10.5194/bg-12-653-2015, 2015.

642 Thomalla, F., and Boyland, M.: Enhancing resilience to extreme climate events:  
643 Lessons from the 2015-2016 El Niño event in Asia and the Pacific. UNESCAP,  
644 Bangkok.

645 van der Werf, G. R., Randerson, J. T., Collatz, G. J., Giglio, L., Kasibhatla, P. S.,  
646 Arellano, A. F., Jr., Olsen, S. C., and Kasischke, E. S.: Continental-scale  
647 partitioning of fire emissions during the 1997 to 2001 El Niño/La Niña period,  
648 *Science*, 303, 73-76, 10.1126/science.1090753, 2004.

649 Wang, J., Zeng, N., and Wang, M.: Interannual variability of the atmospheric CO<sub>2</sub>  
650 growth rate: roles of precipitation and temperature, *Biogeosciences*, 13,  
651 2339-2352, 10.5194/bg-13-2339-2016, 2016.

652 Wang, J., Zeng, N., Wang, M., Jiang, F., Wang, H., and Jiang, Z.: Contrasting  
653 terrestrial carbon cycle responses to the 1997/98 and 2015/16 extreme El Niño  
654 events, *Earth System Dynamics*, 9, 1-14, 10.5194/esd-9-1-2018, 2018.

655 Wang, W., Ciais, P., Nemani, R., Canadell, J. G., Piao, S., Sitch, S., White, M. A.,  
656 Hashimoto, H., Milesi, C., and Myneni, R. B.: Variations in atmospheric CO<sub>2</sub>  
657 growth rates coupled with tropical temperature, *PNAS*, 110, 13061-13066,  
658 10.1073/pnas.1314920110, 2013.

659 Wang, X., Piao, S., Ciais, P., Friedlingstein, P., Myneni, R. B., Cox, P., Heimann, M.,  
660 Miller, J., Peng, S., Wang, T., Yang, H., and Chen, A.: A two-fold increase of

661 carbon cycle sensitivity to tropical temperature variations, *Nature*, 506, 212-215,  
662 10.1038/nature12915, 2014.

663 Wei, Y., Liu, S., Huntzinger, D. N., Michalak, A. M., Viovy, N., Post, W. M., Schwalm,  
664 C. R., Schaefer, K., Jacobson, A. R., Lu, C., Tian, H., Ricciuto, D. M., Cook, R.  
665 B., Mao, J., and Shi, X.: The North American Carbon Program Multi-scale  
666 Synthesis and Terrestrial Model Intercomparison Project – Part 2: Environmental  
667 driver data, *Geosci Model Dev*, 7, 2875-2893, 10.5194/gmd-7-2875-2014, 2014.

668 Weng, H., Ashok, K., Behera, S. K., Rao, S. A., and Yamagata, T.: Impacts of recent  
669 El Niño Modoki on dry/wet conditions in the Pacific rim during boreal summer,  
670 *Climate Dynamics*, 29, 113-129, 10.1007/s00382-007-0234-0, 2007.

671 Weng, H., Behera, S. K., and Yamagata, T.: Anomalous winter climate conditions in  
672 the Pacific rim during recent El Niño Modoki and El Niño events, *Climate  
673 Dynamics*, 32, 663-674, 10.1007/s00382-008-0394-6, 2009.

674 Yeh, S. W., Kug, J. S., Dewitte, B., Kwon, M. H., Kirtman, B. P., and Jin, F. F.: El  
675 Niño in a changing climate, *Nature*, 461, 511-514, 10.1038/nature08316, 2009.

676 Yu, J.-Y., Zou, Y., Kim, S. T., and Lee, T.: The changing impact of El Niño on US  
677 winter temperatures, *Geophys Res Lett*, 39, 10.1029/2012gl052483, 2012.

678 Zaehle, S., and Friend, A. D.: Carbon and nitrogen cycle dynamics in the O-CN land  
679 surface model: 1. Model description, site-scale evaluation, and sensitivity to  
680 parameter estimates, *Global Biogeochemical Cycles*, 24, Artn Gb1005, Doi  
681 10.1029/2009gb003521, 2010.

682 Zeng, N., Mariotti, A., and Wetzel, P.: Terrestrial mechanisms of interannual

683 CO<sub>2</sub>variability, *Global Biogeochemical Cycles*, 19, GB1016,

684 10.1029/2004gb002273, 2005.

685 Zhang, Y., Xiao, X., Guanter, L., Zhou, S., Ciais, P., Joiner, J., Sitch, S., Wu, X.,

686 Nabel, J., Dong, J., Kato, E., Jain, A. K., Wiltshire, A., and Stocker, B. D.:

687 Precipitation and carbon-water coupling jointly control the interannual

688 variability of global land gross primary production, *Sci Rep*, 6, 39748,

689 10.1038/srep39748, 2016.

690

691

692

693

694

695

696

697

698

699

700

701

702

703

704

705



706

707

708

709

## Tables and Figures

710 Table 1 TRENDY models used in this study.

No.	Model	Resolution (lat×lon)	Fire Simulation	References
1	CLM4.5	0.94°×1.25°	yes	Oleson et al., 2013
2	ISAM	0.5°×0.5°	no	Jain et al., 2013
3	JSBACH	1.875°×1.875°	yes	Reick et al., 2013
4	JULES	1.6°×1.875°	no	Clark et al., 2011
5	LPX-Bern	1°×1°	yes	Keller et al., 2017
6	OCN	0.5°×0.5°	no	Zaehle et al., 2010
7	VEGAS	0.5°×0.5°	yes	Zeng et al., 2005
8	VISIT	0.5°×0.5°	yes	Kato et al., 2013

711

712 Table 2 Eastern Pacific (EP) and Central Pacific (CP) El Niño events used in this

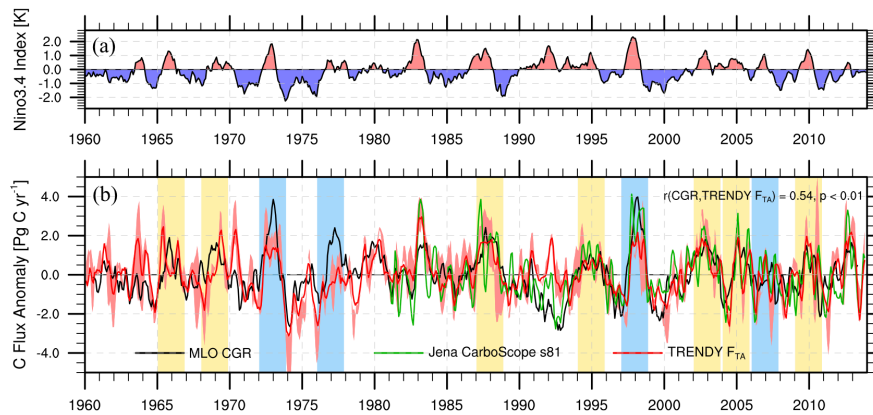
713 study, as identified by a majority consensus of three methods.

<b>EP El Niño</b>	<b>CP El Niño</b>
1972/73	1965/66
1976/77	1968/69
1997/98	1987/88
2006/07	1994/95
	2002/03
	2004/05
	2009/10

714

715

716



717

718 Figure 1. Interannual variability in the Niño3.4 Index and the carbon cycle. (a)

719 Niño3.4. (b) Mauna Loa (MLO) CO<sub>2</sub> growth rate (CGR, black line), as well as

720 TRENDY multi-model median (red line) and Jena inversion (green line) of the global

721 land–atmosphere carbon flux ( $F_{TA}$ , positive value means into the atmosphere, units in

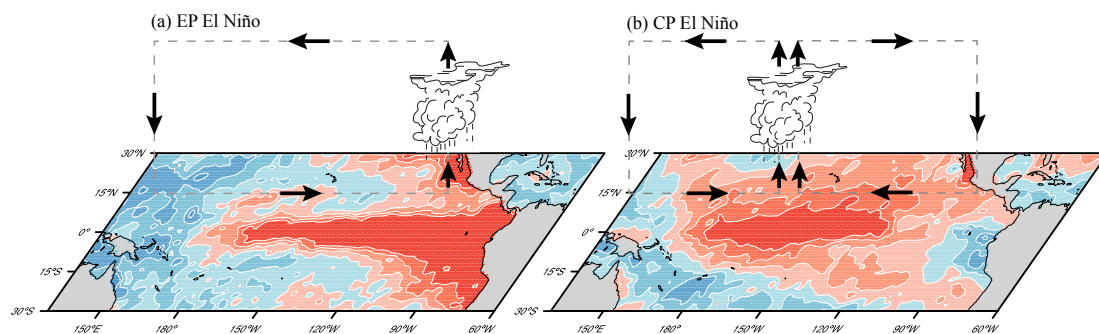
722 Pg C yr<sup>-1</sup>), which were further smoothed by the 3-month running average. The light

723 red shaded represents the area between the 5% and 95% percentiles of the TRENDY

724 simulations. The bars represent the El Niño events selected for this study, with the EP

725 El Niño in blue and the CP El Niño in yellow.

726

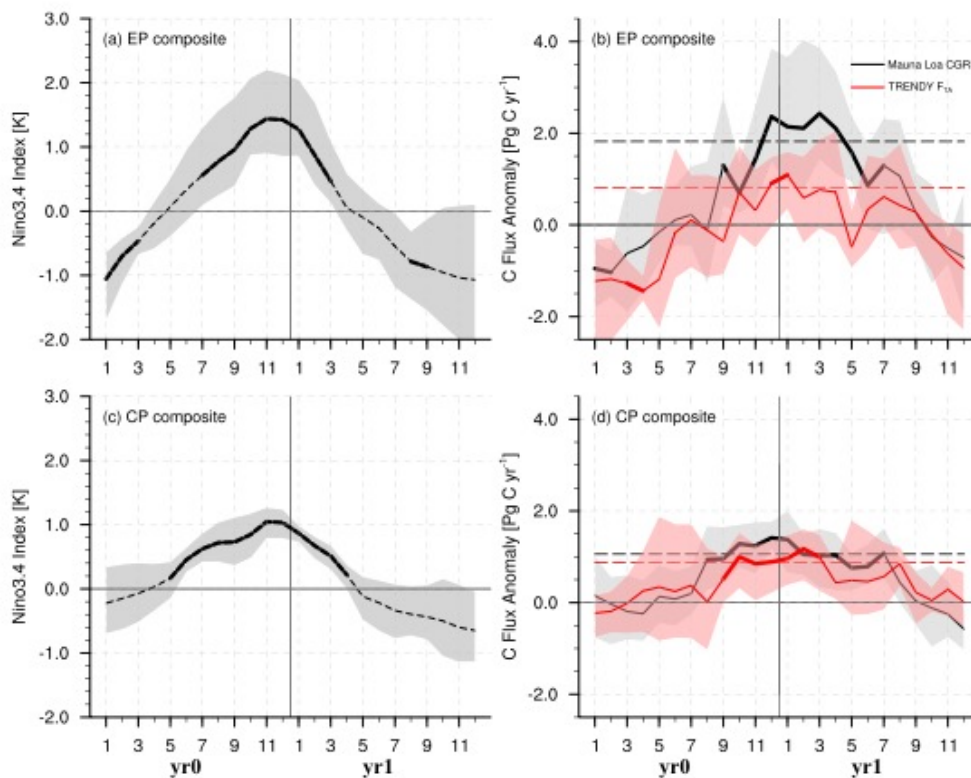


727

728 Figure 2. Schematic diagram of the two types of El Niños. (a) sea surface temperature

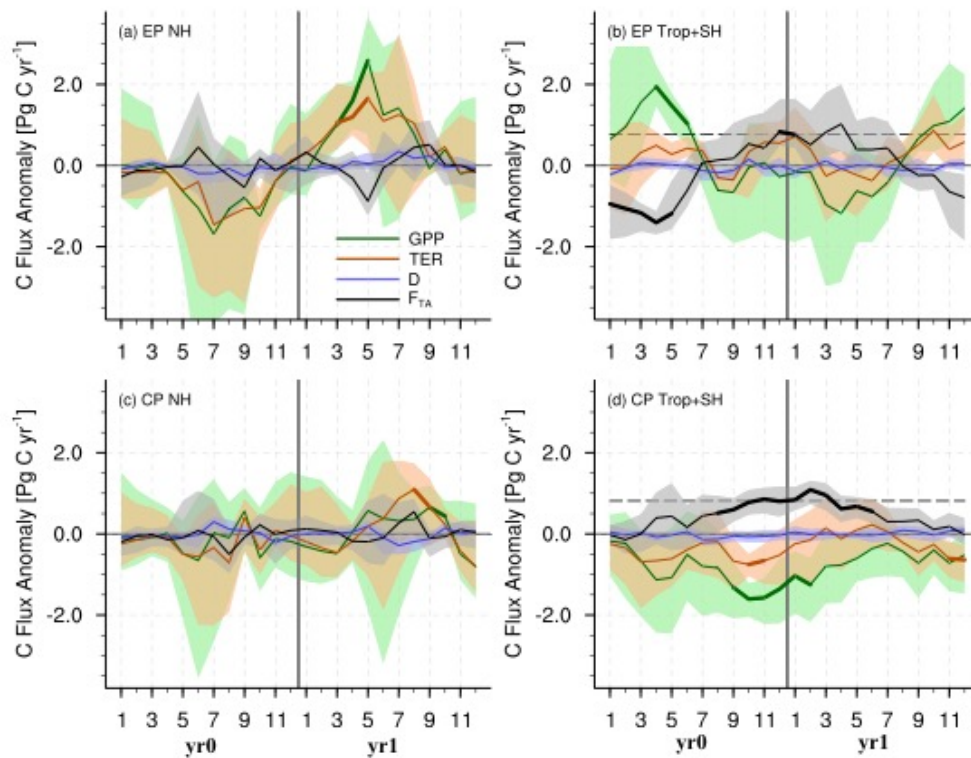
729 anomaly (SSTA) over the tropical Pacific associated with the anomalous Walker  
 730 Circulation in an EP El Niño. (b) SSTA with two cells of the anomalous Walker  
 731 Circulation in a CP El Niño. Red colors indicate warming, and blue colors indicate  
 732 cooling. Vectors denote the wind directions.

733



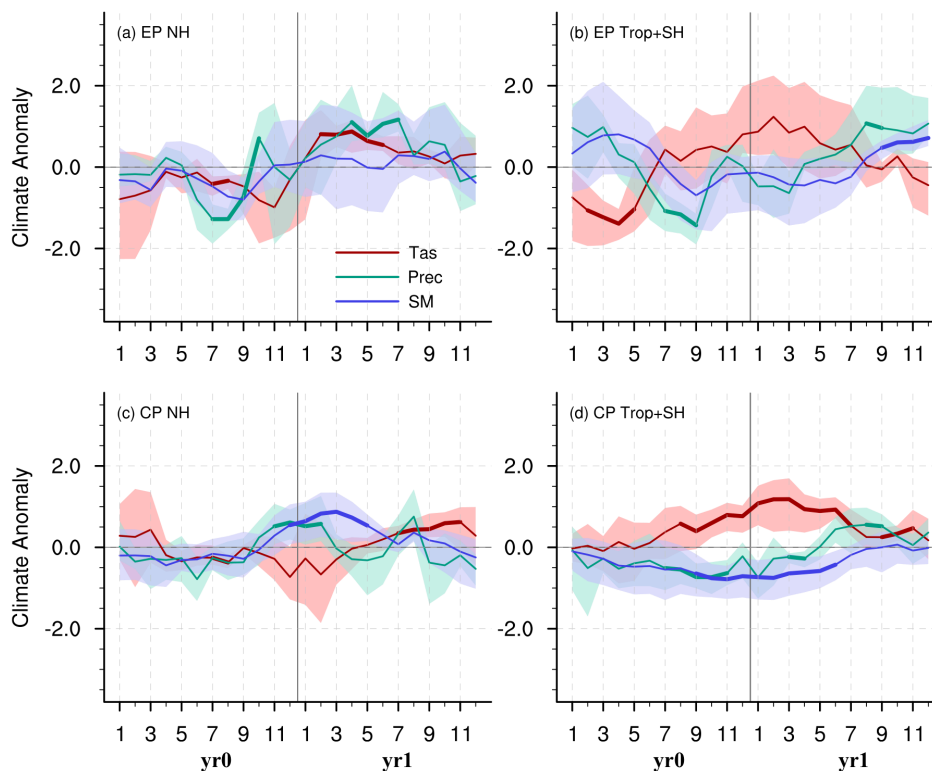
734  
 735 Figure 3. Composites of El Niño and the corresponding carbon flux anomaly (Pg C  
 736 yr<sup>-1</sup>). (a) The Niño3.4 Index composite during EP El Niño events. (b) Corresponding  
 737 MLO CGR and TRENDY v4 global F<sub>TA</sub> composite during EP El Niño events. (c) The  
 738 Niño3.4 Index composite during CP El Niño events. (d) Corresponding MLO CGR  
 739 and TRENDY v4 global F<sub>TA</sub> composite during CP El Niño events. The shaded area  
 740 denotes the 95% confidence intervals of the variables in the composite, derived from

741 1000 bootstrap estimates. The bold lines indicate the significance above the 80% level  
 742 estimated by the Student's *t*-test. The black and red dash lines in b and d represent the  
 743 thresholds of the peak duration (75% of the maximum CGR or  $F_{TA}$  anomaly).  
 744



745  
 746 Figure 4. Composites of anomalies in the TRENDY  $F_{TA}$  (black lines), gross primary  
 747 productivity (GPP, green lines), terrestrial ecosystem respiration (TER, brown lines),  
 748 and the carbon flux caused by disturbances (D, blue lines) during two types of El  
 749 Niños over the extratropical northern hemisphere (NH, 23°N–90°N) and the tropics  
 750 and extratropical southern hemisphere (Trop+SH, 60°S–23°S). The shaded area  
 751 denotes the 95% confidence intervals of the variables in the composite, derived from  
 752 1000 bootstrap estimates. The bold lines indicate the significance above the 80% level  
 753 estimated by the Student's *t*-test. The black dash lines in b and d represent the

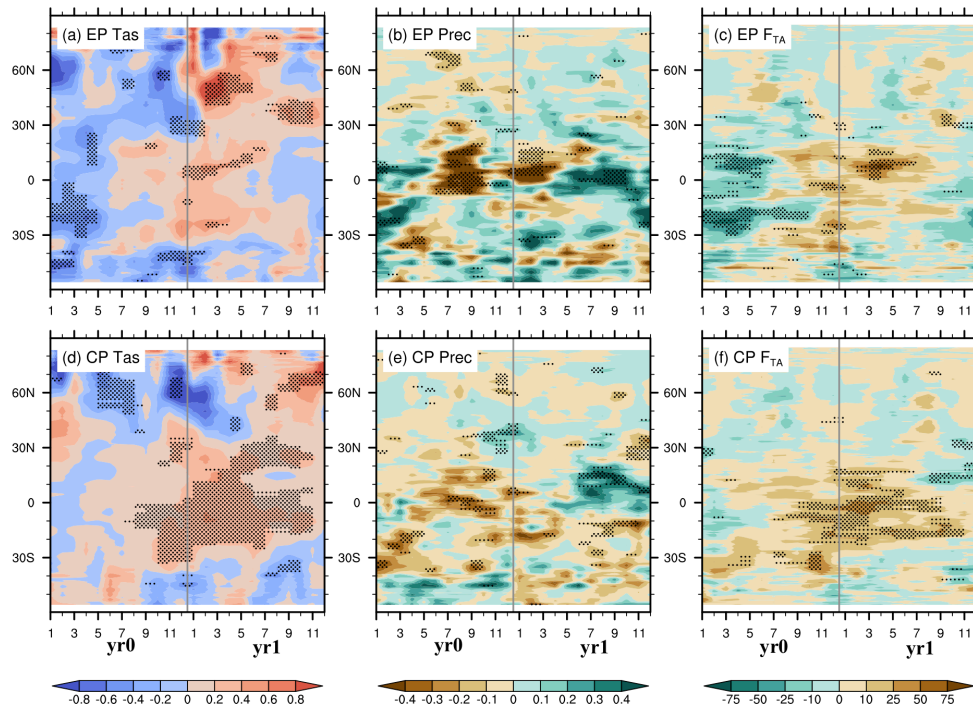
754 thresholds of the peak duration.



755

756 Figure 5. Composites of the standardized land surface air temperature (Tas, red lines),  
757 precipitation (green lines), and TRENDY simulated soil moisture content (SM, blue  
758 lines) anomalies in two types of El Niños over the NH, Trop+SH. Shaded area  
759 denotes the 95% confidence intervals of the variables in the composite, derived in  
760 1000 bootstrap estimates. The bold lines indicate the significance above the 80% level  
761 estimated by Student's *t*-test.

762



763

764 Figure 6. Hovmöller diagrams of the anomalies in climate variables and the  $F_{TA}$

765 (averaged from  $180^{\circ}W$  to  $180^{\circ}E$ ) during EP and CP El Niño events. (a and d) surface

766 air temperature anomalies over land (units: K); (b and e) precipitation anomalies over

767 land (units:  $\text{mm d}^{-1}$ ); (c and f) TRENDY simulated  $F_{TA}$  anomalies (units:  $\text{g C m}^{-2} \text{yr}^{-1}$ )

768 during EP and CP El Niño events. The dotted areas indicate the significance above the

769 80% level as estimated using the Student's  $t$ -test.

770

771